Space-time characteristics of fragment emission in the $E/A = 30$ MeV ^{129}Xe + ^{nat}Cu reaction

D.R. Bowman,[1] N. Colonna,[2] W.A. Friedman,[3] L. Celano,[2] M. D'Agostino,[4] J.D. Dinius,[5] A. Ferrero,[6,*] C.K. Gelbke,[5] T. Glasmacher,[5] D.O. Handzy,[5] D. Horn,[1] W.C. Hsi,[5] M. Huang,[5] I. Iori,[6] M.A. Lisa,[5,†] W.G. Lynch,[5] G.V. Margagliotti,[7] P.M. Milazzo,[4] C.P. Montoya,[5] A. Moroni,[6] G.F. Peaslee,[5,‡] L. Phair,[5,†] F. Petruzzelli,[6] R. Scardaoni,[6] C. Schwarz,[5,§] M.B. Tsang,[5] and C. Williams[5]

[1] *Atomic Energy of Canada, Ltd., Chalk River Laboratories, Chalk River, Ontario, Canada K0J 1J0*

[2] *INFN, Via Amendola 173, 70126 Bari, Italy*

[3] *Department of Physics, University of Wisconsin, Madison, Wisconsin 53706*

[4] *Dipartimento di Fisica and INFN, Via Irnerio 46, 40126 Bologna, Italy*

[5] *NSCL, Michigan State University, East Lansing, Michigan 48824*

[6] *Dipartimento di Fisica and INFN, Via Celoria 12, 20133 Milano, Italy*

[7] *Dipartimento di Fisica and INFN, Via A. Valerio 2, 34127 Trieste, Italy*

(Received 3 February 1995)

Intermediate-mass-fragment emission has been studied in central $E/A = 30$ MeV ^{129}Xe + ^{nat}Cu reactions. The measured fragment multiplicities, reduced-velocity correlation functions, and emission velocities have been compared with schematic three-body trajectory calculations and with three statistical models with input based upon a dynamical BNV code. The statistical models which include expansion either explicitly or implicitly are able to generate a sufficient number of fragments. The three-body trajectory calculations indicate a mean emission time of ≈ 200 fm/c, consistent with sequential decay. Dynamical expanding-emitting source calculations predict a similar time scale for fragment emission and give satisfactory agreement with the experimental correlation functions if the experimental angular distributions are incorporated into the model. The Berlin multifragmentation model gives good agreement with the experimental charge distributions, and, depending upon the choice of radius parameter, can provide agreement with either the correlation functions or the fragment emission velocities, but not with both simultaneously. Although an overall good agreement is obtained in the statistical model comparisons, even in the most violent collisions the angular distributions and fragment emission velocities are incompatible with completely equilibrated decay from a single source.

PACS number(s): 25.70.Pq

I. INTRODUCTION

Studies of IMF (intermediate mass fragment, $3 \leq Z \leq 20$) emission [1] have provided a wealth of information about the space-time extent of excited nuclear systems. At high bombarding energy, $E/A > 100$ MeV, the fragments appear to be emitted on the very short time scale implied by a prompt multifragment disassembly of heated and expanded nuclear systems [2,3]. At low bombarding energy, $E/A < 20$ MeV, standard compound nucleus decay accounts for much of the fragment yield following either complete or incomplete fusion reactions [4–6]. To gain a systematic understanding of the interaction between complex nuclei it is important to characterize the intermediate bombarding energy regime, where the fragment emission time scale changes from sequential to simultaneous [7,8], and nuclear expansion begins to occur [9,10].

Observables which have been employed to infer the spatial and temporal extensions of fragmentation sources are fragment yields, fragment-fragment reduced-velocity correlation functions, and emission velocities of emitted fragments. The IMF yields calculated with statistical emission models are strongly dependent on the density of the emitting system [11–14]. Comparisons of experimental data with model predictions have shown that nuclear expansion is needed to reproduce the observed fragment multiplicities and charge distributions, even at bombarding energies as low as $E/A = 35$ MeV [13]. The fragment emission time scale, as determined from fragment-fragment correlations, is a direct measure of the space-time extent of the source [2,3,7,8,15–26]. The fragment emission velocities are sensitive to an expansion of the source, which leads to a decrease in the Coulomb repulsion energy [10] and to a collective radial velocity, which provides a boost to the emitted fragments [27,28]. Simultaneous measurements of the relative-velocity correlation functions and the fragment emission velocities may allow a distinction between the spatial and temporal extensions

*On leave from the Comisión de Energia Atómica, Argentina.

†Present address: Lawrence Berkeley Laboratory, 1 Cyclotron Rd., Berkeley, CA 94720.

‡Present address: Physics Department, Hope College, Holland, MI 49223.

§Present address: Gesellschaft für Schwerionenforschung, D-64220 Darmstadt, Germany.

of the source [24].

Both equilibrium and nonequilibrium mechanisms contribute to the measured fragment yield at intermediate bombarding energy (20 MeV $\leq E/A \leq$ 100 MeV) [17,29–31]. Results of microscopic transport model calculations for $A \sim 200$ systems at bombarding energies $E/A < 50$ MeV indicate that peripheral collisions lead to projectilelike and targetlike primary fragments through incomplete damping of the entrance-channel kinetic energy, whereas central collisions lead to a composite system through a fusionlike process [32,33]. Studies of these reactions with state-of-the-art 4π detector systems that allow an approximate impact-parameter selection may be able to identify which reaction mechanisms dominate IMF production for different collision geometries. Such a study was performed for $E/A = 35$ MeV ^{36}Ar + ^{197}Au reactions [17]. Although contributions from nonequilibrium emission were found to persist in even the most violent collisions, a much larger degree of equilibration was observed as the centrality of the reaction increased.

In this paper we report on a study of the $E/A =$ 30 MeV ^{129}Xe + ^{nat}Cu system with a low-threshold 4π detector system which allows an event-by-event impact-parameter estimation and has a high efficiency for fragment detection. We primarily confine ourselves to the most violent events where the kinetic energy dissipation and the degree of equilibration is expected to be highest. In contrast to analyses which have focused on one particular aspect of fragment emission, we examine the three observables described above: the IMF multiplicity and charge distributions, the fragment-fragment reduced-velocity correlation function, and the velocity distributions of fragments with $Z = 6$. We compare the data with predictions of a schematic three-body trajectory calculation and with three statistical-decay models which make varying assumptions about the characteristics of the decaying system. It is our expectation that no single model with one set of input parameters will successfully predict all of the features of fragment emission, but that important ingredients in each of the models may be brought forth. Our procedure gives a perspective which is perhaps more balanced than studies focusing on a single aspect of a reaction.

The paper is organized as follows: The experimental details are given in Sec. II, the model calculations are described in Sec. III, the results are presented and discussed in Sec. IV, and a summary is given in Sec. V.

II. EXPERIMENTAL DETAILS

An $E/A = 30$ MeV ^{129}Xe beam of intensity $\sim 3 \times 10^7$ particles/s was delivered by the K1200 Cyclotron of the National Superconducting Cyclotron Laboratory at Michigan State University and impinged upon a target of ^{nat}Cu of 2.4 mg/cm^2 areal density. Charged reaction products were detected from 8° to 23° with 36 elements of the high-resolution gas-Si-Si(Li)-CsI MULTICS array [34], and from 23° to 160° with 158 elements (rings Nos. 3–11) of the MSU Miniball [35]. The complete detector system covered a solid angle greater than 87% of 4π.

Charged particles of $1 \leq Z \leq 54$ were detected with the MULTICS array. Detection thresholds were approximately $E/A = 2.5$ MeV for all fragments, and the resolution in Z was much better than 1 unit for $Z < 30$. For $Z \sim 6$ fragments the probability for misidentification as a neighboring atomic number was $\approx 2\%$. Energy calibrations were performed by directing 18 separate beams into each of the 36 telescopes [36]. The calibration beams had energies of $E/A = 30$ and 70 MeV, and ranged in mass from ^{12}C to ^{129}Xe. An energy resolution of better than 2% was obtained. Position calibrations of the Si elements of the MULTICS array were performed with the procedure of Ref. [37]. The angular resolution was estimated to be $\approx 0.2°$.

Charged particles of $1 \leq Z \leq 20$ were detected with the Miniball. Identification thresholds were approximately $E/A = 2$, 3, and 4 MeV for fragments with $Z = 3$, 10, and 18, respectively. Charged particles with energies below the identification threshold and above $E/A > 1$ MeV were detected, but not identified. Miniball detectors at angles $\theta > 100°$ had larger solid angles and therefore required foils (5.05 mg/cm^2 of a Pb-Sn alloy) for electron suppression. These foils increased the energy thresholds by approximately 20%. The resolution in Z was better than 1 unit for $Z \leq 6$ and typically ± 1 unit for $7 \leq Z \leq 20$. The Z resolution was strongly dependent upon fragment energy; peak-to-valley ratios were typically better than 5:1 for $Z < 10$ fragments with energies $E/A < 5$ MeV. The resolution became progressively poorer with increasing energy. During the experiment the Miniball was cooled and temperature stabilized. Drifts in the phototube gains were monitored with a light-pulser system and found to be less than 2%. Absolute energy calibrations were obtained by normalizing the measured proton punch-through points of 75.2 MeV to existing calibration curves [38]. The energy calibrations were estimated to be accurate to $\sim$10% at forward angles where the punch-through points were well identified and accurate to $\sim$20% for more backward ($\theta > 80°$) angles where they were not.

The nuclear reaction probability for IMF's which traverse the entire length of the MULTICS Si(Li) detectors is approximately 2%. The reaction probability for particles which punch through the Miniball CsI detectors (essentially only protons) is about 7%. For lower-energy fragments with smaller ranges (> 98% of all fragments and particles), the reaction probabilities are smaller.

Data were taken on two conditions: (i) At least two Miniball elements were triggered, or (ii) at least one fragment of $Z > 2$ was detected in the MULTICS array. More than 92% of the events that satisfied condition (ii) also satisfied condition (i). Because of the low beam intensity, the random coincidence rate from different events was less than 0.1%. Events which satisfied either of the two conditions were written to magnetic tape in an event-by-event format. Calibrations were performed off line and the results written in an event-by-event sequence to new tapes with parameters of Z, energy, θ, and ϕ.

III. MODELS EMPLOYED

To test the statistical emission hypothesis, we have compared the experimental data with predictions from

three statistical-decay codes, each of which rely on different assumptions about the space-time characteristics of the fragmenting system. Rather than attempting to fit the data by choosing optimal values for the many parameters in these models, we have used a set of reasonable and consistent assumptions for each calculation. Our procedure is described in this section.

The code GEMINI [6] calculates sequential binary emission of all species ranging from nucleons to symmetric fission fragments. Light particles are treated with the evaporation formalism [39] and fragments of $Z > 2$ with the transition state model of Ref. [40]. There are no three-body correlations in the GEMINI. Each binary decay product is assumed to be fully accelerated by the Coulomb field of its partner before the succeeding particle or fragment is emitted. Therefore, the calculated fragment-fragment reduced-velocity correlation function, which tests the space-time extent of the emitting source, should not be thought of as a realistic prediction for sequential binary decay, but rather as a limit for an infinite time between steps in the decay chain.

The expanding-emitting source model (EES) of Friedman [41] treats surface evaporation of light particles and fragments ($Z \leq 9$) with the binary evaporation formalism. Both emission probabilities and expansion or contraction of the source are calculated as a function of time. An effective compressibility is built into the model through the following relationship between binding energy and density:

$$E(\rho)/A = E_{LD}(\rho_0)/A + (K/18)[1 - (\rho/\rho_0)]^2. \quad (1)$$

Here $E_{LD}(\rho_0)/A$ is the binding energy at normal nuclear density. We choose the finite-nucleus compressibility K to be 144 MeV. This corresponds to a "soft equation of state."

The Berlin multifragmentation model (BMM) [42] calculates the simultaneous statistical disassembly of a nuclear system inside a volume characterized by a radius $R_{FO} = r_0 A^{1/3}$. Typically the parameter r_0 is set to be approximately 2.1 fm. In one set of calculations, r_0 was increased to 2.6 fm to provide agreement with fragment-fragment correlation functions measured in peripheral reactions at $E/A = 50$ MeV [23].

To estimate of the properties of an equilibrated source, we have used the BNV (Boltzmann-Nordheim-Vlasov) model of Ref. [43] to simulate the early dynamical stage of the collision [13,14,32,33,44,45]. The BNV model allows for preequilibrium emission of light particles which can decrease the excitation energy in the residue [46,47]. Calculations at an impact parameter of b=0 fm were followed to times of 140 fm/c.[1] An infinite nuclear matter compressibility K_∞ of 200 MeV was used in these calculations. This also corresponds to a "soft equation of state." The mass loss, source density, excitation energy, and collective radial energy [44] predicted by the BNV calculation are shown as a function of time in Fig. 1.

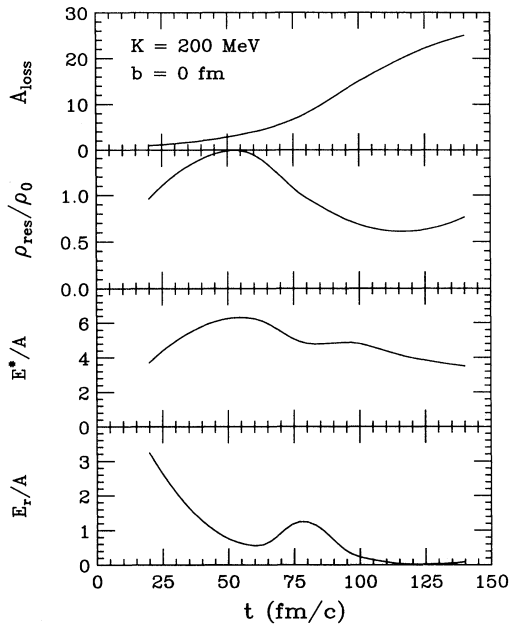

FIG. 1. BNV predictions for b=0 fm ^{129}Xe + ^{nat}Cu collisions with a compressibility parameter K = 200 MeV. The predicted mass loss (top panel), density of the residue (second panel), excitation energy per nucleon in the residue (third panel), and collective radial energy per nucleon in the residue (bottom panel) are shown as a function of time.

The source properties for GEMINI and the EES model were determined at the time when the nuclear matter returned to normal density following compression (≈80 fm/c). Since these models assume spherical symmetry, a radial decomposition of the matter distribution predicted by the BNV model was performed [44,45]. The average binding energies of spherical shells of 1 fm thickness were estimated. Two sets of input parameters were then extracted: the first including all bound shells (R_S=8 fm) and the second including all bound shells and the first "unbound" shell (R_S=9 fm). The charge, mass, thermal excitation energy, and collective radial energy were used as input for the EES calculations. Only a single set of input parameters was used in the GEMINI calculations corresponding to the higher excitation energy case R_S=9 fm. Because GEMINI does not allow expansion, the excitation energy was taken to be the sum of the thermal and radial expansion energies. A triangular angular momentum distribution between 0 and 70$\hbar$ was used in the GEMINI calculations.[2]

The BMM assumes fragment formation from a nuclear system at low density. Therefore, the coupling with the dynamical calculation was chosen to be at the point

[1] At t=0 the projectile and target surfaces are separated by approximately 2 fm.

[2] In the calculation, 70$\hbar$ is the maximum angular momentum the source can sustain with a nonzero fission barrier. BNV calculations at b=4 fm [the impact parameter bounding the most central 14% of the geometric cross section (see below)] give angular momenta greater than 70$\hbar$.

TABLE I. Parameters for statistical model calculations: time of the coupling, source (freeze-out) radius, charge, mass, excitation energy, and energy of radial expansion, and the mean fragment multiplicities calculated with each model.

	τ (fm/c)	r (fm)	Z	A	E^* (MeV)	E_R (MeV)	$\langle N_{\rm IMF}\rangle$
GEMINI	80	9	77	175	860	-	0.4
EES	80	9	77	175	700	160	2.0 (0.9)
EES	80	8	73	165	540	130	1.1 (0.7)
BMM	115	14.6	76	177	750	-	2.4
BMM	115	11.8	76	177	750	-	2.3

of maximum expansion (t=115 fm/c, ρ/ρ_0=0.6) [32,33]. Two calculations were performed with the BMM: the first with a standard radius parameter of 2.1 fm ($R_{\rm FO}$=11.8 fm) and the second with an extended radius parameter of 2.6 fm ($R_{\rm FO}$=14.6 fm). The values of the parameters used in the statistical model calculations are listed in Table I.

IV. RESULTS AND DISCUSSION

A. Charged-particle and fragment multiplicities

The measured charged-particle multiplicity N_C distribution (Fig. 2, top), which includes particles detected but not identified, shows a broad, flat region extending to multiplicities of approximately 13 and a sharply falling tail at larger multiplicities. An approximate impact-parameter scale is given at the top of the figure [48], where $b_{\rm max}$ is the impact parameter corresponding to the minimum-bias trigger, N_C=2. The relationship between the average detected IMF multiplicity ($3 \le Z \le 20$) and the measured charged particle multiplicity is shown in the bottom panel of Fig. 2. The average IMF multiplicity is strongly correlated with N_C up to charged-particle multiplicities of about 15. Beyond this value, the average IMF multiplicity saturates at a value of approximately 1.7. For the highest measured values of N_C, in this case $N_C > 15$, the charged-particle multiplicity is no longer a good indicator of impact parameter or energy deposition [49]. In this paper, we will concentrate on the most violent events with $N_C \ge 14$, which correspond to the upper 14% of the multiplicity distribution, and to reduced impact parameters of $b/b_{\rm max} < 0.37$.

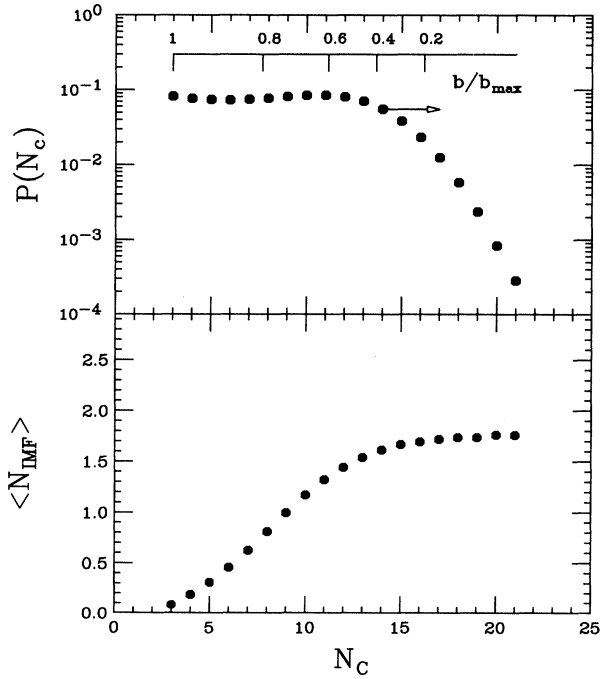

FIG. 2. Top: detected charged-particle multiplicity distribution. An approximate geometrical impact-parameter scale is given at the top of the figure. The arrow indicates the region to which the theoretical calculations were compared. Bottom: relationship between the detected charged-particle multiplicity and the detected IMF ($3 \ge Z \ge 20$) multiplicity.

The measured (solid points) and predicted (curves) IMF multiplicity distributions for events with $N_C \ge 14$ are shown in Fig. 3. The detector acceptance and efficiency have been taken into account in the predictions (filtered calculations). The GEMINI calculation (solid curve) underpredicts the probabilities for multiplicities $N_{\rm IMF} > 1$ by one or more orders of magnitude. The region spanned by the two EES calculations is indicated by horizontal hatching. These two calculations bracket

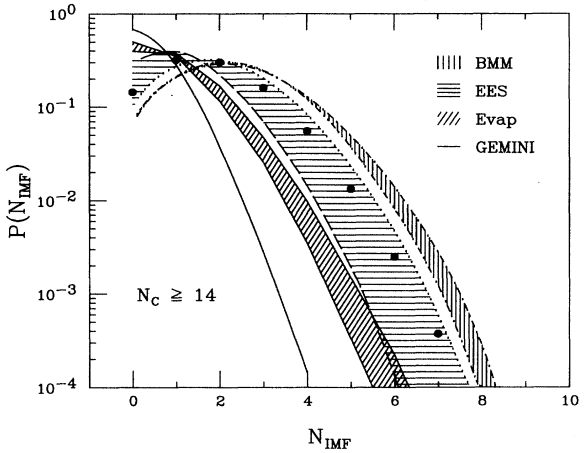

FIG. 3. Probability distribution for the detected intermediate-mass-fragment multiplicity in $N_C \ge 14$ events. The solid points indicate the measured data. The solid line corresponds to GEMINI predictions. The vertically hatched, horizontally hatched, and crosshatched regions correspond to BMM, EES (with expansion), and EES (without expansion) calculations, respectively.

the data. The region spanned by the BMM calculations is indicated by the vertical hatching. These calculations overpredict multiplicities $N_{\mathrm{IMF}} > 2$ by approximately a factor of 2. EES calculations which do not allow expansion ("Evap") are indicated by the angled hatching. In these calculations, probabilities for $N_{\mathrm{IMF}} \geq 2$ are predicted to be smaller than observed by more than a factor of 2. As found in reactions at higher bombarding energy, it is necessary to allow expansion either implicitly (BMM) or explicitly (EES) in order to generate an adequate number of fragments [11–14]. However, the difference between the calculations with and without expansion is much smaller than that observed at higher energy.

The IMF charge distribution measured in events with $N_C \geq 14$ is shown by the solid points in Fig. 4. The experimental charge distribution exhibits a steep decrease for $3 \leq Z \leq 10$ and a more gradual falloff for larger atomic numbers. Raw and filtered calculations with the BMM model and with GEMINI are depicted by the dot-dashed and solid curves, respectively.

The BMM calculations (Fig. 4, top and middle panels) give good qualitative agreement with the experimental charge distributions over the entire atomic number range of $3 \leq Z \leq 40$. Conversely, the GEMINI calculation (bottom panel) underpredicts the yields of fragments of $Z \leq 6$ by an order of magnitude and predicts a nearly flat charge distribution.

Calculations with the EES model are compared with

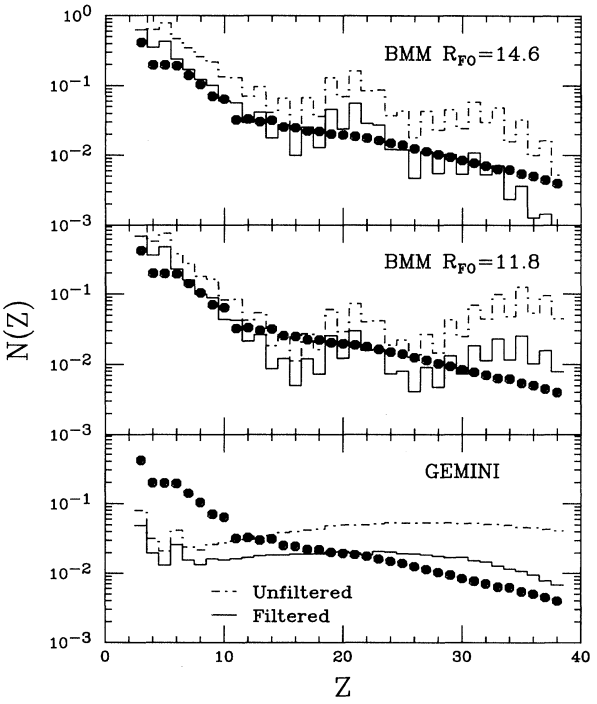

FIG. 4. Experimental charge distribution (solid points) in $N_C \geq 14$ events compared with unfiltered (dot-dashed curves) and filtered (solid curves) predictions by the BMM model with a freeze-out radius of $R_{\mathrm{FO}} = 14.6$ fm (top panel), the BMM model with a freeze-out radius of $R_{\mathrm{FO}} = 11.8$ fm (central panel), and GEMINI (bottom panel).

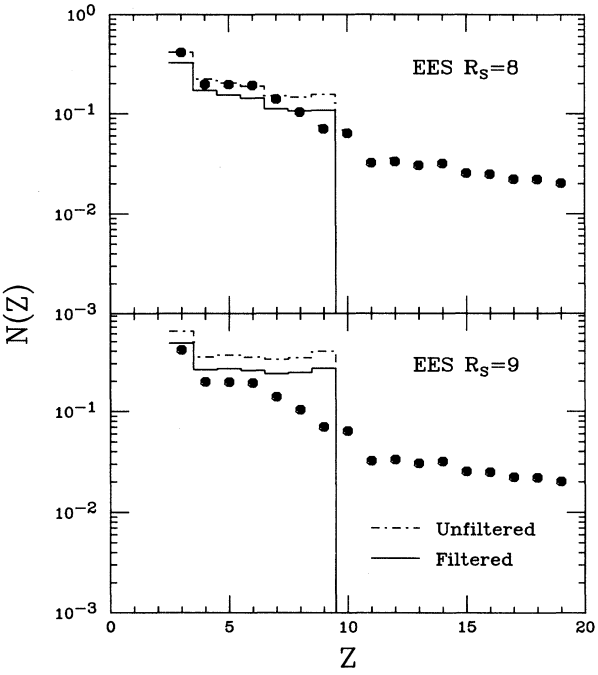

FIG. 5. Experimental charge distribution (solid points) in $N_C \geq 14$ events compared with unfiltered (dot-dashed curves) and filtered (solid curves) predictions by the EES model with an initial source radius of $R_S = 8$ fm (top panel), and the EES model with an initial source radius of $R_S = 9$ fm (bottom panel).

the data in Fig. 5. This model does not allow emission of fragments heavier than $Z = 9$. The shape of the experimental charge distribution is best reproduced by the EES calculation with $R_S = 8$ fm (top panel). The calculation with $R_S = 9$ fm (bottom panel) systematically overpredicts the measured fragment yields. The greatly overpredicted yields for $7 \leq Z \leq 9$ may be a consequence of the increased expansion which occurs in the calculation with the larger initial radius. In the EES model, there is an energy gain ("coalescence heating") associated with the emission of heavy fragments from dilute systems [41].

The magnitude of the fragment yields suggest that expansion may be important even at $E/A = 30$ MeV or that other dynamical effects not treated in the statistical models provide enhanced fragment emission.

B. Correlation functions

Determination of the fragment emission time scale may provide further information about the disassembly mechanism. In order to obtain a measure of this time scale we have evaluated the experimental two-fragment ($4 \leq Z \leq 9$) reduced-velocity correlation function [3,7,8,17–24]

$$1 + R(V_{\mathrm{red}}) = C \frac{\sum Y(\mathbf{v}_1, \mathbf{v}_2)}{\sum Y(\mathbf{v}_1) Y(\mathbf{v}_2)}. \quad (2)$$

Here $Y(\mathbf{v}_1, \mathbf{v}_2)$ is the coincidence yield of fragments with

velocities $\mathbf{v}_1$ and $\mathbf{v}_2$,[3] and $Y(\mathbf{v}_1)$ and $Y(\mathbf{v}_2)$ are the singles yields of fragments with the corresponding velocities. The distributions in the denominator were constructed by selecting $\mathbf{v}_1$ and $\mathbf{v}_2$ values from different events ("event-mixing technique"). The reduced relative velocity $V_{\rm red} = |\mathbf{v}_1 - \mathbf{v}_2| / \sqrt{Z_1 + Z_2}$ is introduced to eliminate the charge dependence of the fragment-fragment relative velocity in mixed-fragment correlation functions [18]. The factor C is a normalization constant equal to the ratio of the total denominator events to the total numerator events. This is the normalization procedure of choice for fragment-fragment analyses where correlations exist at large relative velocity due to energy and momentum conservation [22,23]. Fragments detected with the high-resolution MULTICS array — approximately 37% of all fragments detected in $N_C \geq 14$ events — provided data for the correlation functions.

The experimental correlation function (Fig. 6) exhibits a depletion for $V_{\rm red} < 0.015c$, which is sensitive to the space-time distribution of coincident fragments, and an enhancement at $V_{\rm red} = 0.018c$. Because of the normalization procedure employed, the anticorrelation observed for $V_{\rm red} < 0.015c$ requires a corresponding enhancement in the correlation function where $1+R > 1$.

In Fig. 6, the data are compared with schematic, three-body trajectory calculations described in Ref. [24].[4]

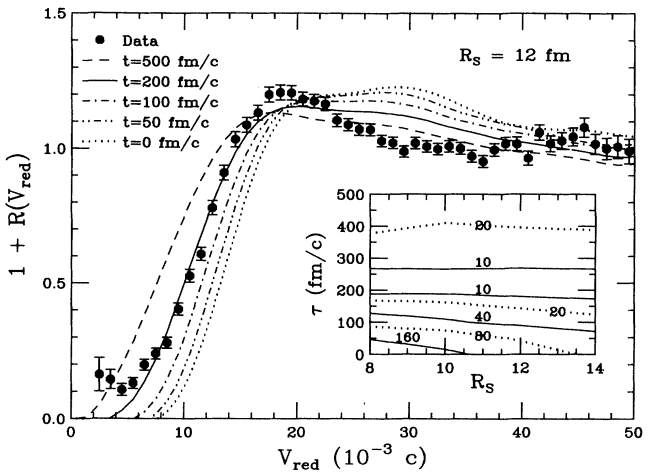

FIG. 6. Comparison of experimental ($N_C \geq 14$) fragment-fragment reduced-velocity correlation functions (solid points) with three-body trajectory calculations (curves). The calculations were performed assuming a source radius R_S of 12 fm and the indicated mean emission times τ. Inset: contours of chi-squared per degree of freedom for three-body trajectory calculations in τ-R_S space. Solid contours correspond to levels of 10, 40, and 160. Dotted contours correspond to levels of 20 and 80.

[3]The laboratory velocities were calculated from the measured atomic numbers and energies assuming a fragment mass of $A = 2Z$.

[4]The code described herein reproduces the calculations of Refs. [7,17–19].

The calculations assumed a source radius of $R_S = 12$ fm and various mean emission times ranging from 0 to 500 fm/c. The source charge $Z_S = 77$, source mass $A_S = 175$, and source velocity $\mathbf{V}_S = 0.17c$ were determined from the BNV calculations, and the experimental energy and angular distributions were sampled. The calculated correlation functions exhibit an increase with $V_{\rm red}$ for $V_{\rm red} < 0.018c$, which is similar in shape to the data. For $V_{\rm red} > 0.018c$, the calculated and experimental correlation functions have different shapes, as the calculations underpredict the magnitude of the peak at $V_{\rm red} = 0.018c$ and overpredict the correlation function at $0.025c < V_{\rm red} < 0.04c$. The magnitude of the calculated enhancement near $V_{\rm red} = 0.03c$ is correlated with the depletion at $V_{\rm red} < 0.015c$.

The best agreement with the data is obtained for an emission time of τ=200 fm/c (solid curve). To quantify the level of agreement, reduced chi-squared values between the data and the calculations were determined over the rising portion of the correlation function, $0.004c \leq V_{\rm red} \leq 0.017c$, where the calculated and experimental correlation functions have similar shapes. However, for any range of $V_{\rm red}$ that includes the rising portion of the correlation function, the agreement with data is superior for the $\tau = 200$ fm/c calculation.

A contour plot of the reduced chi-squared values versus τ and R_S is shown as an inset in the figure. For all assumed source radii between 8 and 14 fm, a mean emission time of 200 fm/c gives the best agreement with the data. The calculated correlation functions are sensitive to the assumed radius parameter for emission time scales $\lesssim 100$ fm/c; for longer time scales, the calculations become insensitive to R_S. The deduced time scale of 200 fm/c is consistent with that of sequential decay. We note that a ^{12}C fragment with a kinetic energy of 13 MeV (approximately twice the predicted temperature of the ^{129}Xe + $^{\rm nat}$Cu system in a central collision) will travel a distance corresponding to 1.75 times its diameter in a time of 200 fm/c.

Simulations of complex multiparticle final states with three-body trajectory calculations are a gross simplification of the decay process. We have investigated the dependence of the calculated correlation functions on the assumptions and parameters within the simulations.

In the three-body trajectory calculations, the initial energy of the emitted fragments, prior to Coulomb acceleration, is taken to be

$$E_{\rm init} = \frac{m}{2} |\mathbf{v}_{\rm lab} - \mathbf{V}_S|^2 - E_{\rm Coul}. \quad (3)$$

Here m is the fragment mass; $\mathbf{v}_{\rm lab}$ is the measured fragment velocity vector determined by a Monte Carlo sampling of the experimental energy and angular distributions; $\mathbf{V}_S$ is the source velocity vector, assumed from the BNV calculations to have a magnitude of 0.17c directed along the beam axis; and $E_{\rm Coul}$ is an estimated Coulomb repulsion energy calculated from the source charge Z_S, fragment charge $Z_{\rm frag}$, and the source radius R_S as

$$E_{\rm Coul} = \frac{1.44 Z_S Z_{\rm frag}}{R_S + R_{\rm frag}}. \quad (4)$$

The fragment radius $R_{\rm frag}$ is taken to be $1.2A_{\rm frag}^{1/3}$. This simple two-sphere parametrization of the decay configuration neglects thermal shape fluctuations at the scission point [40,50] and polarization of the charge during the decay process, which could decrease the emission energy as in the case of low-energy binary fission [51].

For some fraction of the experimental energy spectra, the calculated value of $E_{\rm init}$ is < 0 ("subbarrier emission"). In the three-body trajectory code these events are discarded and the measured energy spectra are sampled again. The percentage of the experimental energy spectra that is sampled depends upon the values of the parameters Z_S and R_S. The correlation functions with $R_S = 12$ and 14 fm and $Z_S = 25$, 40, 50, and 77 are shown in Fig. 7. In these calculations, the initial source mass predicted by the BNV simulations, $A_S = 175$, has been scaled with the source charge. The enhancement near $V_{\rm red} = 0.020c$ becomes progressively more attenuated as Z_S decreases, but for $V_{\rm red} < 0.015c$ the correlation functions are similar for the calculations with $Z_S > 25$. In contrast, the sampled fractions of the energy distribution are very sensitive to the value of Z_S. These fractions range from 0.4 to 0.90 for $Z_S = 77$–40. This demonstrates that time scales extracted from the rising portions of the correlation functions are not very dependent on the initial energy distribution.

The calculated correlation functions at $V_{\rm red} > 0.015c$ are, however, quite sensitive to the charge and mass of the emitting source. An enhancement at $V_{\rm red} \sim 0.035c$ dominates the correlation functions with $Z_S = 25$. This enhancement is imposed by momentum conservation in the less massive source. If the source mass is kept fixed at a value of 175, then the correlation functions calculated with $Z_S = 25$ become flat for $V_{\rm red} > 0.018c$.

An enhancement at lower reduced velocity, near $V_{\rm red} = 0.020c$, dominates the correlation functions with $Z_S \geq 40$. This enhancement is seen in the present data and has been observed previously [19–21]. It has been theoretically attributed to the primary importance of the fragment-fragment Coulomb interaction in the correlation function, as opposed to the influence of three-body and higher-order correlations [22], and experimentally attributed to the existence of a heavy residue in the final state [21]. We have investigated the nature of this feature with the three-body trajectory calculations. Although the magnitude of the enhancements in Fig. 7 appears to depend strongly on Z_S, in fact, we find that the dependence is on the initial thermal energy of the nascent fragments. A decrease in Z_S in Eq. (4) leads to an increase in the initial fragment energies $E_{\rm init}$ in (3). As the initial energies increase, the peak due to the fragment-fragment Coulomb interaction becomes progressively attenuated. Modifying the source charge to $Z_S = 25$ while constraining $E_{\rm init}$ to values similar to those obtained with $Z_S = 77$ gives a similar enhancement as for the $Z_S = 77$ case. Other parameters also affect the magnitude of the enhancement. Modifying the source velocity can attenuate the peak through Eq. (3), and, as shown in [21], simulating a longer time scale attenuates the peak by giving larger fragment-fragment separations in coordinate space.

Although the correlation function at $V_{\rm red} > 0.018c$ is dependent upon the choice of A_S, Z_S, and $\mathbf{V}_S$, the rising portion of the correlation function at $V_{\rm red} < 0.018c$ is quite independent of these parameters. Small modifications of A_S, Z_S, R_S, and $\mathbf{V}_S$ can improve the agreement between data and calculations over that shown in Figs. 6 and 7, but an overprediction is always observed in the range of $0.025c < V_{\rm red} < 0.035c$. While this region of the correlation functions is not understood quantitatively, for all choices of A_S, Z_S, R_S, and $\mathbf{V}_S$ we obtain the best agreement between data and calculations with a fragment emission time scale of 200 fm/c.

One may also set thresholds on the experimental energy spectra and study correlations between fragments with emission energies "above the barrier" [24]. In reverse kinematics reactions, where the source moves with a large velocity, it is necessary to transform into the source frame before setting the energy threshold. The correlation function for fragments with energies of $E/A > 2.5$ MeV in the source frame (see below) is shown as the open points in Fig. 8.[5] These events with two or more high-energy fragments correspond to $\approx 13\%$ of all two-fragment events detected with the MULTICS array. The curves in Fig. 8 depict calculations with the three-body

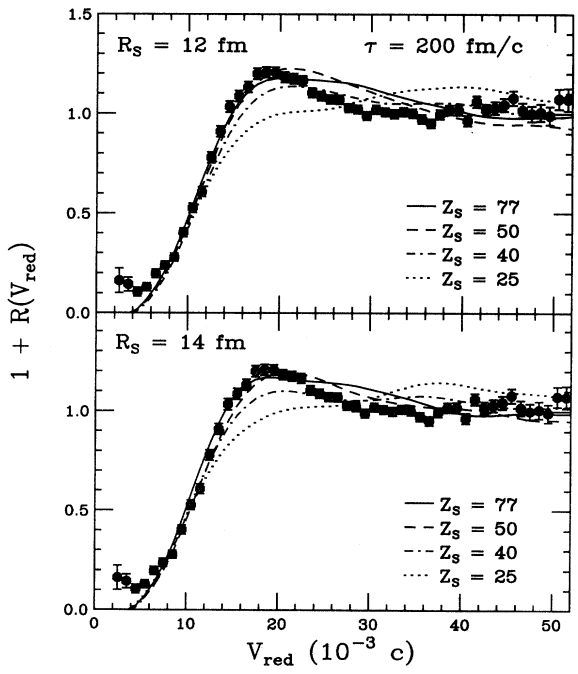

FIG. 7. Correlation functions predicted by three-body trajectory calculations with source charges of $Z_S = 77$, 50, 40, and 25 and source radii of $R_S = 12$ fm (top) and $R_S = 14$ fm (bottom) for a mean fragment emission time of 200 fm/c.

[5] A laboratory frame threshold of $E/A > 6$ MeV was employed in Ref. [24]. At a laboratory angle of 20°, this threshold corresponds to $E/A = 2.2$ MeV in the center-of-mass frame, and is therefore similar to what was used in the present work.

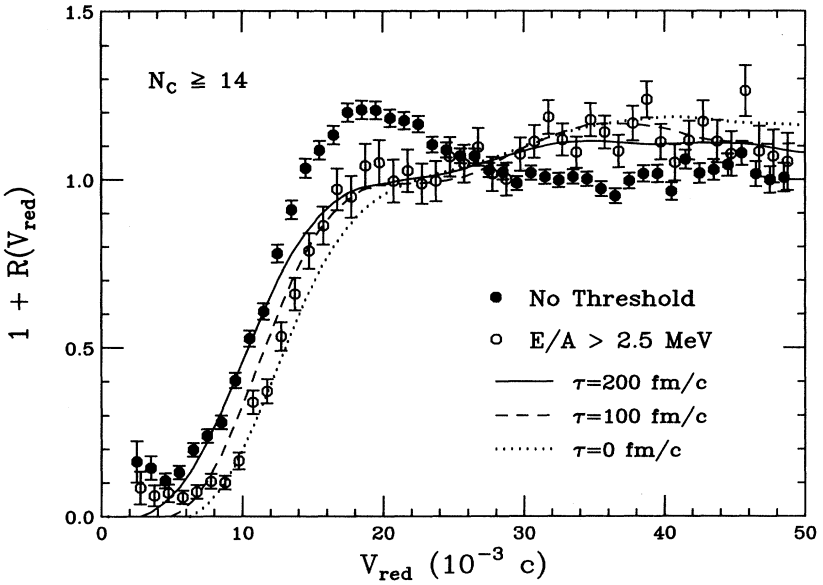

FIG. 8. Fragment-fragment reduced-velocity correlation functions in $N_C \geq 14$ events for all fragments of $4 \geq Z \geq 9$ (solid points), and for fragments of $4 \geq Z \geq 9$ with energies $E/A > 2.5$ MeV in the average source frame (open points). The curves correspond to three-body trajectory calculations with a source radius of $R_S = 12$ fm and mean emission times of 200 (solid curve), 100 (dashed curve), and 0 (dotted curve) fm/c for fragments with energies greater than 2.5 MeV.

trajectory code for a source charge of 50, a source radius of 12 fm, and mean emission times of 200 (solid curve), 100 (dashed curve), and 0 (dotted curve) fm/c after applying the same energy threshold. (Approximately 43% of the simulated events passes the threshold.) Note that the energy-gated correlation function has a significantly different shape than the ungated correlation function, and that the three-body trajectory simulations provide good agreement over the entire range of $V_{\rm red}$. Comparison of the gated correlation function with the simulations indicates a faster emission time scale $0 \leq \tau \leq 100$ fm/c for these higher-energy fragments. These fragments can be understood as originating early in the decay chain from systems with higher temperature and more charge (hence, increased Coulomb emission energy). Previous work has also indicated a smaller emission time for fragments of higher energy [17,24].

The inclusive fragment emission time scale of $\approx$ 200 fm/c can be directly compared with the mean emission time calculated with the EES model. Mean emission times of ~190 fm/c and ~110 fm/c were calculated for the two cases with initial radii of 8 fm and 9 fm, respectively. The mean emission time for the R_S=8 fm case, determined solely from the input parameters provided by the BNV calculations, agrees quantitatively with the experimental emission time determined from the trajectory calculations.

In Fig. 9 the experimental correlation function is compared with calculations generated by the three statistical decay models. For the GEMINI and BMM calculations the simulated-event files were filtered through a software replica of the MULTICS array. For the EES calculations the three-body trajectory code described above was modified to generate correlation functions based on the theoretical charge distributions, emission time distributions, and the (time-dependent) source charge, mass, temperature, and radius. These calculated events were then

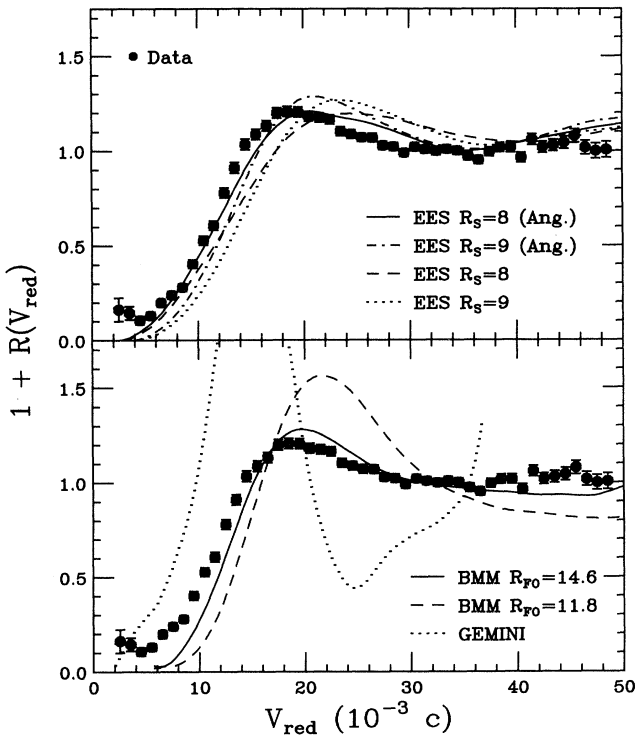

FIG. 9. Comparison of experimental ($N_C \geq 14$) fragment-fragment reduced-velocity correlation functions (solid points) with filtered statistical model calculations. Top: EES with R_S=8 fm and experimental angular distribution (solid curve), R_S=9 fm and experimental angular distribution (dot-dashed curve), R_S=8 fm and isotropic angular distributions (dashed curve), and R_S=9 fm and isotropic angular distributions (dotted curve). Bottom: BMM with $R_{\rm FO}$=14.6 fm (solid curve), BMM with $R_{\rm FO}$=11.8 fm (dashed curve), and GEMINI (dotted curve).

passed through the experimental filter. In the top panel, correlation functions based upon the R_S=8 fm (dashed curve) and R_S=9 fm (dotted curve) EES calculations are shown. Although the calculated emission times agree well with those determined from the trajectory calculations, the correlation functions exhibit differences. Because the angular distributions assumed in the EES model do not correspond to the experimental angular distributions (see below), the initial positioning of the fragments in the EES and trajectory calculations differs. This difference in initial conditions has a discernible effect on the calculated correlation functions.

The direction of the initial radius vector of each fragment was chosen according to Lambert's law for surface emission, $P(\theta) \propto \cos\theta$, where θ is the angle between the radius vector and the previously determined velocity vector. Hence, different angular distributions of the fragments result in different initial spatial distributions.

Replacing the isotropic angular distributions assumed by the EES model with the experimental angular distributions leads to the correlation functions shown in Fig. 9 by the solid (R_S=8 fm) and dot-dashed (R_S=9 fm) curves. The agreement of these calculations with the data is much improved, demonstrating that realistic single-particle distributions must be used for quantitative analyses of correlation functions.

The bottom panel of Fig. 9 shows the correlation functions predicted by GEMINI and the BMM model. The GEMINI calculation (dotted curve), which assumes an infinite time between emissions, gives an incorrect shape. Approximately one-half of the coincident fragment-fragment pairs predicted by GEMINI are formed by the binary splitting of a primary parent. This process gives rise to a well-defined relative velocity between the two IMF's and a strong peak in the correlation function that is not observed in the data.

The BMM calculation with the standard radius of 11.8 fm (dashed curve) also gives poor agreement with the data. Better agreement is obtained (solid curve) with a larger radius of R_S = 14.6 fm, as observed for peripheral collisions at E/A = 50 MeV [23]. However, because of the dual sensitivity of the correlation function to space and time, such a large radius may be unrealistic and mimic a finite lifetime that is not considered in the BMM model. To determine if simultaneous fragment emission from a greatly expanded system is realistic, we examine the fragment emission patterns predicted by the different decay models in the following section.

C. Velocity and angular distributions

A widely used technique for isolating the sources contributing to fragment emission is to plot the cross section in velocity space for a given atomic number as $d^2\sigma/dv_\parallel dv_\perp$ [5,6,19,29,46,52]. This is a particularly powerful technique when a global observable such as the charged-particle multiplicity or the total detected charge is used as an event selector. For example, in the ^{139}La + ^{nat}Ni reaction at E/A = 18 MeV [5] the total detected charge was used to select a range of momentum-mass transfers in the incomplete fusion process and to demonstrate the simple, binary nature of the decay; in the ^{129}Xe+ ^{nat}Cu reaction at E/A = 50 MeV, multiplicity-gated velocity distributions were used to demonstrate the evolution of the reaction mechanism from the sequential decay of projectilelike and targetlike fragments in peripheral reactions to the fast disassembly of a single anisotropic "source" in central collisions [19].

We now examine the distribution of C fragments in velocity space in order to determine the degree of relaxation of the kinetic energy and angular degrees of freedom. Statistical models stipulate that the angular distributions of the fragments be forward-backward symmetric in the frame of the decaying system. The predicted emission velocities are determined primarily by the Coulomb repulsion energy between the emitted fragment and the residual system, and are independent of emission angle.

In the upper left-hand panel of Fig. 10 the experimental distribution of C fragments in velocity space is shown for events with $N_C \geq 14$. The discontinuities in the distribution are caused by detector acceptance effects; for laboratory angles > 23° the events have been randomized over the face of the struck Miniball detector. There is a depletion of events centered approximately at $v_\parallel$ = 0.17c, $v_\perp$ = 0c, which corresponds nearly to the center-of-mass velocity of the system (arrow). Such a "Coulomb hole" is a signature of binary decay of a system with a sharply defined velocity and a significant charge, and is consistent with a statistical emission process. The dis-

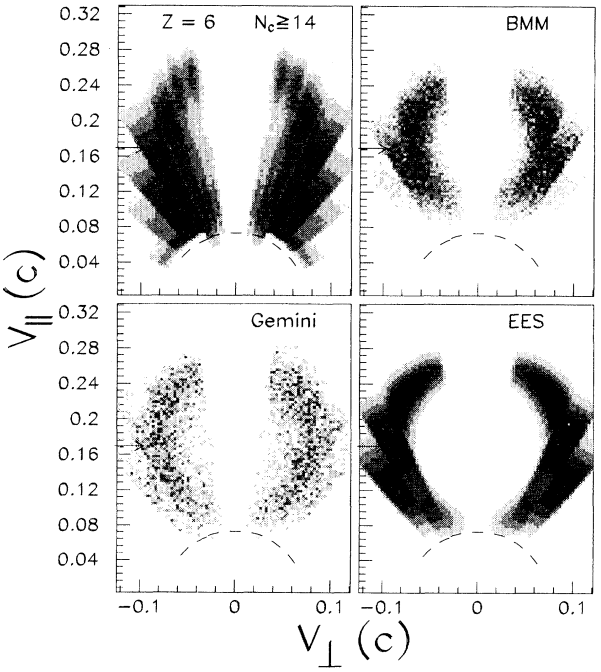

FIG. 10. Linear density plots of the cross section in velocity space $d^2\sigma/dv_\parallel dv_\perp$ for Z = 6 emission in $N_C \geq 14$ events. Upper left, experimental data; upper right, BMM model; lower left, GEMINI; lower right, EES model. The approximate low-energy threshold is depicted by the dashed lines. The center-of-mass velocity is indicated by the arrows.

tribution of events around the Coulomb hole, however, is not isotropic. There are more events at backward angles in the frame of the decaying system than at forward angles.

In order to characterize the emission patterns more quantitatively, we have employed the coincident-fragment source-velocity technique developed in Ref. [5] to determine the average velocity of the decaying system:

$$\mathbf{V}_S = \frac{\sum_{i=1}^{N_{\rm frag}} \mathbf{p}_i}{\sum_{i=1}^{N_{\rm frag}} m_i}. \quad (5)$$

A detected charge of $Z_{\rm total} > 35$ was required to exclude events in which only a small fraction of the momentum was measured. The source velocity distributions are shown in Fig. 11 for threefold, fourfold, and fivefold fragment ($Z > 2$) events. The mean and standard deviation of the integrated distribution were determined to be $0.174c$ and $0.015c$, respectively. This average source velocity corresponds to nearly full (92%) momentum transfer in the simple incomplete fusion model.

The distributions of C fragments in velocity space predicted by the statistical decay models are shown in Fig. 10 [panels (b), (c), and (d)] after boosting by the average source velocity and filtering through the experimental acceptance. As required by the statistical emission hypothesis, the calculated velocity distributions exhibit well-defined Coulomb holes and Coulomb circles and forward-backward symmetric angular distribution which are not observed in the data. The radii of the predicted circles depends mainly upon the Coulomb energy of the decay configuration, which in turn depends upon the assumed breakup geometry in each of the models (see below).

The experimental data were transformed event by event into the average source frame determined from the source velocity distribution. The solid points in Fig. 12 (top) depict the angular distribution of C fragments in this frame as a differential multiplicity, namely, fragments per event per radian. The yield rises slowly with angle beyond 30° and reaches a pronounced maximum near 150°. Assuming that all of the fragments emitted forward of 90 degrees arise from fully relaxed statistical emission, the forward-backward ratio of the differential cross section can be used to estimate the degree of equilibration of the angular degrees of freedom [29]. Such a decomposition for angles of $30° - 150°$ gives an equilibrium fraction of $\approx$78% for $N_C \geq 14$ events. The open points in the top panel of Fig. 12 depict the experimental angular distribution for events with $N_C \geq 19$, which corresponds to $\sim$0.4% of the total number of events with $N_C > 2$. The equilibrium fraction of C fragments in these events is $\approx$85%. Thus, gating on the extreme tail of the charged-particle multiplicity distribution selects a more equilibrated set of events; however, complete relaxation of the angular degrees of freedom is still not observed.

The angular distribution of C fragments predicted by the EES model with $R_S = 8$ fm is indicated by the dot-dashed curve in the top panel of Fig. 12. This angular distribution is isotropic ($dP/d\Omega = \text{const}$, $dP/d\theta \propto \sin\theta$) in the source frame and is similar in shape to those predicted by the other statistical models, except at very small and very large angles where detector acceptance effects are encountered. The agreement of the predicted angular distributions with the data is excellent for emission angles $< 90°$ (there is no normalization factor between theory and data), but the backward peaking observed in the experimental distribution is inconsistent

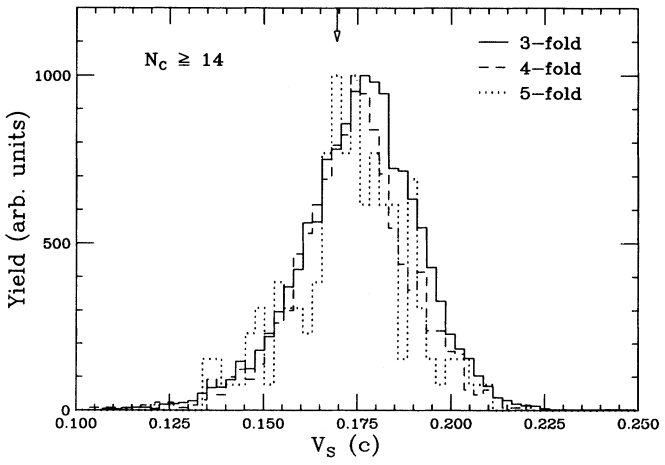

FIG. 11. Source velocity distributions for the indicated number of $Z \geq 3$ fragments in $N_C \geq 14$ events with a total detected charge of $Z_{\rm total} > 35$.

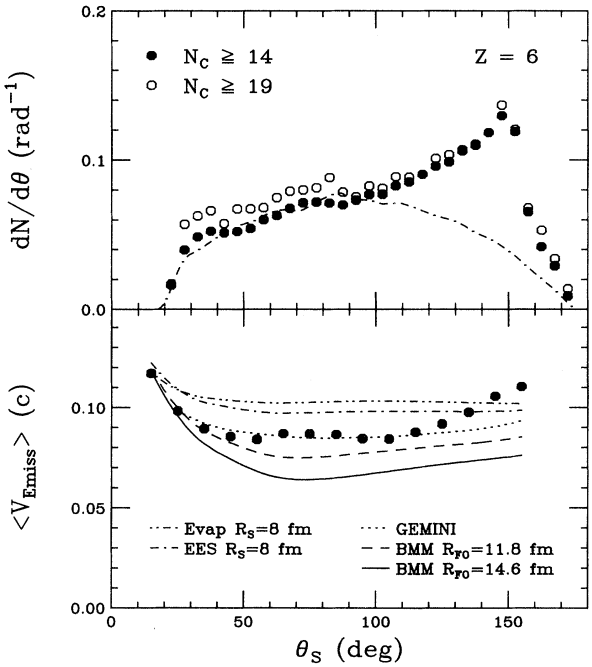

FIG. 12. Top: angular distributions in the source frame for $N_C \geq 14$ (solid points) and $N_C \geq 19$ events (open points). The curve corresponds to a prediction by the EES model with R_S=8 fm. Bottom: the average (solid points) emission velocities in the source frame ($\mathbf{V}_S$=0.174c) as a function of emission angle in $N_C \geq 14$ events. The curves correspond to filtered calculations with the indicated statistical models.

with equilibrium statistical decay from a single source, which requires forward-backward symmetric decay patterns.

The mean emission velocities of C fragments are shown in Fig. 12 (bottom) as a function of emission angle in the source frame. The nearly constant values of $V_{\rm emiss}$ over the range of θ_S=35°–115° are consistent with equilibrium emission. The larger values of $V_{\rm emiss}$ at small θ_S are caused by the experimental acceptance (note the similarity of the data and the statistical model calculations described below). The increase at larger θ_S is indicative of the additional component of fragment emission which was apparent in the source-frame angular distributions.

The enhancement in the differential cross section at backward angles, > 100°, signifies the existence of fragments with either a targetlike or a neck origin [53,54]. The mean emission velocities of these fragments are too large to be explained by equilibrium emission from a fusionlike source.

After boosting by the average source velocity and filtering through the response of the experimental apparatus, the calculated mean emission velocities of C fragments are presented in the bottom panel of Fig. 12. The two EES calculations (R_S = 8 fm shown) overpredict the average emission velocity in the θ_S range where equilibrium emission dominates. An EES calculation that does not allow expansion ("Evap") overpredicts the data even more greatly. The GEMINI calculation shows good agreement with the data, whereas the BMM calculation with a radius of 11.8 fm underpredicts and that with a radius of 14.6 fm greatly underpredicts the average emission velocities.

The predicted emission velocities are smaller for the BMM calculations with a larger radius because of the decreased Coulomb energy of the expanded decay configuration. There is a trade-off in the BMM calculations between providing good agreement with the fragment-fragment correlation functions (larger radius) or providing better agreement with the fragment emission velocities (smaller radius). The lack of a concerted good agreement indicates that simultaneous decay as assumed by the BMM model is an unlikely scenario. The mechanism is apparently characterized by an effective radius smaller than 14.6 fm and by a finite lifetime.

In the EES model, the emission energy consists of Coulomb, thermal, and collective components. The Coulomb energy is calculated by a simple two-sphere parametrization for binary decay. The Coulomb component is

$$E_{\rm Coul} = \frac{e^2 Z_{\rm res} Z_{\rm frag}}{1.2(R_{\rm res} + R_{\rm frag})}, \tag{6}$$

where $Z_{\rm frag}$ and $Z_{\rm res}$ are the atomic numbers of the emitted fragment and the residual nucleus, respectively; $R_{\rm res}$ is the (time-dependent) radius of the emitting source; and $R_{\rm frag}$ is the radius of the emitted fragment ($= 1.2A_{\rm frag}^{1/3}$). The thermal contribution to the emission energy follows a Maxwell distribution $P(E_{\rm therm}) \propto E_{\rm therm} e^{-E_{\rm therm}/T}$. The collective component results from the expansion or contraction of the source. For fragment emission, the bulk of the emission energy is contained in the Coulomb component.

An EES calculation which does not allow expansion ("Evap") predicts larger emission velocities because of the increased Coulomb energy in the more compact decay configuration. The collective radial velocity of expansion in the standard EES calculations is not enough to offset the increase in Coulomb energy. The EES calculations with R_S=9 fm predict slightly smaller Coulomb energies and slightly larger radial energies than those with R_S=8 fm because of the greater expansion of the source. However, the calculated emission velocities are nearly identical for the two initial source radii.

In GEMINI the emission energy consists of Coulomb and rotational components. The Coulomb component is

$$E_{\rm Coul} = \frac{1.44 Z_{\rm frag} Z_{\rm res}}{1.16(A_{\rm frag}^{1/3} + A_{\rm res}^{1/3}) + 2}, \tag{7}$$

where $Z_{\rm frag}$, $Z_{\rm res}$, and $A_{\rm frag}$ are defined as above, and $A_{\rm res}$ is the mass number of the residual nucleus. The rotational component depends upon the orbital angular momentum of emission, J, and contributes little to the total emission energy. GEMINI also allows for sequential decay of the excited primary fragments which leads to a reduction in the average emission velocity for a given atomic number.

The better agreement predicted by GEMINI appears to result from the empirical radius parametrization (2 fm separation between partners), which reproduces the low-energy binary-decay systematics [4,29]. This parametrization may mimic the shape polarization effects mentioned above which decrease the average Coulomb energies. A realistic treatment of such polarization effects requires a dynamical description of fragment emission [55–59]. A reduction of the Coulomb barrier in the EES model by 10% for the R_S = 8 fm calculation also provides improved agreement with the measured IMF multiplicity distribution (Fig. 3) and the mean C emission velocity (Fig. 12), with only a slight decrease in the predicted emission times (τ = 180 fm/c).

V. SUMMARY

We have studied central ($N_C \geq 14$) collisions of ^{129}Xe with $^{\rm nat}$Cu. The experimental data has been compared with three statistical models with input based upon a dynamical BNV code. Standard values of the parameters in each model were employed with no attempt to adjust them to optimize the agreement with the data. Calculations with the binary decay model GEMINI drastically underpredict the fragment multiplicity. In contrast, the models which allow expansion either explicitly (EES) or implicitly (BMM) are able to generate an adequate number of fragments. This result suggests that expansion or other dynamical effects may be important for the production of fragments in this reaction.

The EES model predicts an approximately correct mean fragment emission time, as determined by the trajectory calculations, but the correlation function is not

well reproduced. Use of the experimental angular distributions improves the agreement with the experimental correlation functions. This illustrates the need for models to reproduce single-particle observables as well as more complex quantities.

The multiparticle phase space BMM model gives good agreement with the experimental charge distribution. Varying the radius parameter in this model can provide good agreement with the fragment-fragment correlation function (large radius simulating a finite lifetime) or improved agreement with the fragment emission velocities (standard radius), but not with both simultaneously. This result corroborates the analysis of the fragment-fragment reduced-velocity correlations with three-body trajectory calculations, which indicates a mean fragment emission time of $\approx$ 200 fm/c and signifies a sequential emission time scale.

The experimental angular distributions and the emission velocities of C fragments were found to be inconsistent with fully equilibrated statistical emission from a single source. The mean emission velocities of C fragments show best agreement with the predictions of GEMINI, probably because this model employs an empirical parametrization of the decay radius based upon low-energy systematics. An extended radius parameter may mimic shape polarization effects which lead to the low fragment velocities observed in low-energy fission. In order to allow for such polarization effects and to provide for nonequilibrium emission mechanisms, dynamical models of fragment formation are required [55–59].

This work was supported by the National Science Foundation under Grants Nos. PHY-90-15255 and PHY-92-14992.

[1] L.G. Moretto and G.J. Wozniak, Annu. Rev. Nucl. Part. Sci. **43**, 379 (1993), and references therein.
[2] V. Lips *et al.*, Phys. Lett. B **338**, 141 (1994).
[3] B. Kämpfer *et al.*, Phys. Rev. C **48**, R955 (1993).
[4] L.G. Sobotka, M.A. McMahan, R.J. McDonald, C. Signarbieux, G.J. Wozniak, M.L. Padgett, J.H. Gu, Z.H. Liu, Z.Q. Yao, and L.G. Moretto, Phys. Rev. Lett. **53**, 2004 (1984).
[5] N. Colonna *et al.*, Phys. Rev. Lett. **62**, 1833 (1989).
[6] R.J. Charity *et al.*, Nucl. Phys. **A483**, 371 (1988).
[7] D. Fox *et al.*, Phys. Rev. C **47**, R421 (1993); **48**, 3135(E) (1993).
[8] E. Bauge *et al.*, Phys. Rev. Lett. **70**, 3705 (1993).
[9] R.T. de Souza *et al.*, Phys. Lett. B **300**, 29 (1993).
[10] K. Kwiatkowski, W.A. Friedman, L.W. Woo, V.E. Viola, E.C. Pollacco, C. Volant, and S.J. Yennello, Phys. Rev. C **49**, 1516 (1994).
[11] D.R. Bowman *et al.*, Phys. Rev. Lett. **67**, 1527 (1991).
[12] R.T. de Souza *et al.*, Phys. Lett. B **268**, 6 (1991).
[13] K. Hagel *et al.*, Phys. Rev. Lett. **68**, 2141 (1992).
[14] J. Hubele *et al.*, Phys. Rev. C **46**, R1577 (1992).
[15] R. Bougault, J. Colin, F. Delaunay, A. Genoux-Lubain, A. Hajfani, C. Le Brun, J.F. Lecolley, M. Louvel, and J.C. Steckmeyer, Phys. Lett. B **232**, 291 (1989).
[16] R. Trockel *et al.*, Phys. Rev. Lett. **59**, 2844 (1987).
[17] Y.D. Kim, R.T. de Souza, D.R. Bowman, N. Carlin, C.K. Gelbke, W.G. Gong, W.G. Lynch, L. Phair, M.B. Tsang, and F. Zhu, Phys. Rev. Lett. **67**, 14 (1991); Phys. Rev. C **45**, 338 (1992).
[18] Y.D. Kim, R.T. de Souza, C.K. Gelbke, W.G. Gong, and S. Pratt, Phys. Rev. C **45**, 387 (1992).
[19] D.R. Bowman *et al.*, Phys. Rev. Lett. **70**, 3534 (1993).
[20] T.C. Sangster, M. Begemann-Blaich, T. Blaich, H.C. Britt, A. Elmaani, N.N. Ajitanand, and M.N. Namboodiri, Phys. Rev. C **47**, R2457 (1993).
[21] T.C. Sangster, M. Begemann-Blaich, Th. Blaich, H.C. Britt, L.F. Hansen, M.N. Namboodiri, and G. Peilert, Phys. Rev. C **51**, 1280 (1995).
[22] O. Schapiro, A.R. DeAngelis, and D.H.E. Gross, Nucl. Phys. **A568**, 333 (1994).
[23] O. Schapiro and D.H.E. Gross, Nucl. Phys. **A573**, 143 (1994).
[24] T. Glasmacher *et al.*, Phys. Rev. C **50**, 952 (1994).
[25] O. Lopez *et al.*, Phys. Lett. B **315**, 34 (1993).
[26] M. Louvel *et al.*, Phys. Lett B **320**, 221 (1994).
[27] S.C. Jeong *et al.*, Phys. Rev. Lett. **72**, 3468 (1994).
[28] W.C. Hsi *et al.*, Phys. Rev. Lett. **73**, 3367 (1994).
[29] R.J. Charity, D.R. Bowman, Z.H. Liu, R.J. McDonald, M.A. McMahan, G.J. Wozniak, L.G. Moretto, S. Bradley, W.L. Kehoe, and A.C. Mignerey, Nucl. Phys. **A476**, 516 (1988).
[30] D.E. Fields *et al.*, Phys. Lett. B **220**, 356 (1989).
[31] J.L. Wile *et al.*, Phys. Rev. C **45**, 2300 (1992).
[32] M. Colonna, P. Roussel-Chomaz, N. Colonna, M. Di Toro, L.G. Moretto, and G.J. Wozniak, Phys. Lett. B **283**, 180 (1992).
[33] M. Colonna, N. Colonna, A. Bonasera, and M. Di Toro, Nucl. Phys. **A541**, 295 (1992).
[34] I. Iori *et al.*, Nucl. Instrum. Methods A **325**, 458 (1993).
[35] R.T. de Souza *et al.*, Nucl. Instrum. Methods A **295**, 109 (1990).
[36] M.A. McMahan, G.J. Wozniak, C.M. Lyneis, D.R. Bowman, R.J. Charity, Z.H. Liu, L.G. Moretto, W.L. Kehoe, A.C. Mignerey, and M.N. Namboodiri, Nucl. Instrum. Methods A **253**, 1 (1986).
[37] N. Colonna and E. Lisi, Nucl. Instrum. Methods A **334**, 551 (1994).
[38] C. Schwarz, W.C. Hsi, M.J. Huang, D.R. Bowman, Y.D. Kim, W.G. Lynch, L. Phair, and M.B. Tsang, National Superconducting Cyclotron Laboratory Annual Report, 1993, p. 248.
[39] H. Hauser and H. Feshbach, Phys. Rev. **87**, 366 (1952).
[40] L.G. Moretto, Phys. Lett. **40B**, 185 (1972); Nucl. Phys. **A247**, 211 (1975).
[41] W.A. Friedman, Phys. Rev. Lett. **60**, 2125 (1988).
[42] D.H.E. Gross, Rep. Prog. Phys. **53**, 605 (1990).
[43] A. Bonasera *et al.*, Phys. Lett. B **221**, 233 (1989).
[44] D.R. Bowman *et al.*, Phys. Rev. C **46**, 1834 (1992).
[45] W.J. Llope *et al.*, Phys. Rev. C **51**, 1325 (1995).
[46] K. Hanold, L.G. Moretto, G.F. Peaslee, G.J. Wozniak, D.R. Bowman, M.F. Mohar, and D.J. Morrissey, Phys. Rev. C **48**, 723 (1993).
[47] B. Lott *et al.*, Z. Phys. A **346**, 201 (1993).
[48] C. Cavata, M. Demoulins, J. Gosset, M.C. Lemaire, D.

L'Hote, J. Poitou, and O. Valette, Phys. Rev. C **42**, 1760 (1990).
[49] A. Del Zoppo *et al.*, Phys. Rev. C **49**, 3334 (1994).
[50] L.G. Moretto and D.R. Bowman, in *Proceedings of the XXV International Winter Meeting on Nuclear Physics*, Bormio, Italy, edited by I. Iori (Ricerca Scientifica ed Educazione Permanente, Milan, Italy, 1987), Suppl. 91.
[51] V.E. Viola, Jr., K. Kwiatkowski, and M. Walker, Phys. Rev. C **31**, 1550 (1985).
[52] P. Roussel-Chomaz *et al.*, Nucl. Phys. **A551**, 508 (1993).
[53] L.G. Sobotka, Phys. Rev. C **50**, R1272 (1994).
[54] C.P. Montoya *et al.*, Phys. Rev. Lett. **73**, 3070 (1994).
[55] J. Aichelin, G. Peilert, A. Bohnet, A. Rosenhauer, H. Stöcker, and W. Greiner, Phys. Rev. C **37**, 2451 (1988).
[56] D.H. Boal and J.N. Glosli, Phys. Rev. C **38**, 1870 (1988); **38**, 2621 (1988).
[57] G. Peilert, H. Stöcker, W. Greiner, A. Rosenhauer, A. Bohnet, and J. Aichelin, Phys. Rev. C **39**, 1402 (1989).
[58] H. Feldmeier, Nucl. Phys. **A515**, 147 (1990).
[59] G.F. Burgio, Ph. Chomaz, and J. Randrup, Nucl. Phys. **A529**, 157 (1991).

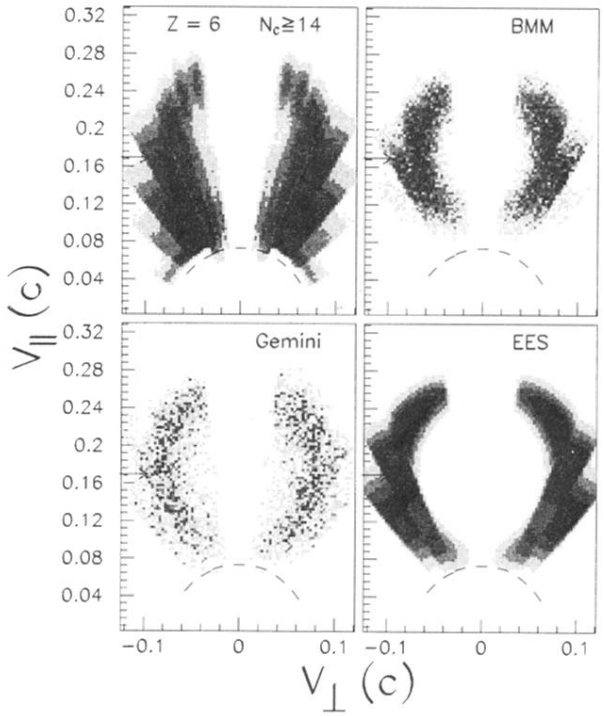

FIG. 10. Linear density plots of the cross section in velocity space $d^2\sigma/dv_\parallel dv_\perp$ for $Z = 6$ emission in $N_C \geq 14$ events. Upper left, experimental data; upper right, BMM model; lower left, GEMINI; lower right, EES model. The approximate low-energy threshold is depicted by the dashed lines. The center-of-mass velocity is indicated by the arrows.